Electrochimica Acta 341 (2020) 135973

Contents lists available at ScienceDirect

Electrochimica Acta

journal homepage: www.elsevier.com/locate/electacta

Designing of nanoflakes anchored nanotubes-like $MnCo_2S_4$/halloysite composites for advanced battery like supercapacitor application

S.K. Shinde [a], G.S. Ghodake [a], N.C. Maile [b], H.M. Yadav [c], A.D. Jagadale [d], M.B. Jalak [e], A.A. Kadam [f], Sivalingam Ramesh [g], C. Bathula [h], D.-Y. Kim [a, *]

[a] Department of Biological and Environmental Science, College of Life Science and Biotechnology, Dongguk University, 32 Dongguk-ro, Biomedical Campus, Ilsandong-gu, Siksa-dong, 10326, Goyang-si, Gyeonggi-do, South Korea
[b] Department of Environmental Engineering, Kyungpook National University, 80 Daehak-ro, Buk-gu, Daegu, 41566, South Korea
[c] Department of Energy and Materials Engineering, Dongguk University, 04620, South Korea
[d] Center for Energy Storage and Conversion, School of Electrical and Electronics Engineering, SASTRA Deemed University, Thanjavur, 613401, Tamilnadu, India
[e] Department of Physics, Shivaji University, Kolhapur, 416004, Maharashtra, India
[f] Research Institute of Biotechnology and Medical Converged Science, Dongguk University, Biomedical Campus, Ilsandong-gu, Goyang-si, Gyeonggi-do, 10326, South Korea
[g] Department of Mechanical, Robotics and Energy Engineering, Dongguk University, 04620, South Korea
[h] Division of Electronics and Electrical Engineering, Dongguk University –Seoul, Pil-dong, Jung-gu, 04620, Seoul, South Korea

ARTICLE INFO

Article history:
Received 17 August 2019
Received in revised form
14 February 2020
Accepted 24 February 2020
Available online 2 March 2020

Keywords:
$MnCo_2S_4$/HNTs composite
Coprecipitation
Screen printing method
Nanotubes
Symmetric electrode

ABSTRACT

In this study, we report a facile chemical synthesis of a novel $MnCo_2S_4$/halloysite (HNTs) nanoflakes decorated on nanotubes which coated on Ni foam via a screen-printing technique. The $MnCo_2S_4$ thin films were prepared using a coprecipitation method which demonstrate battery kind of behavior. The $MnCo_2S_4$/HNTs-based electrode shows a specific capacity of 359 mAh g^{-1} at 5 mV s^{-1} with excellent cycling stability. Furthermore, the symmetric system exhibits an outstanding energy density and power density of 6.98 Wh kg^{-1} and 1976.0 W kg^{-1}, respectively. The results obtained with the $MnCo_2S_4$/HNTs composite in a symmetric system indicate that this composite material can potentially be used as an alternative electrode material for electrochemical energy storage.

1. Introduction

In recent years, world pollution has rapidly increased, necessitating the development of alternative energy sources and storage schemes. Although the existing energy sources and storage techniques are convenient, they face various limitations such as low abundance and poor renewability [1–5]. Examples of non-renewable energy sources include fuels such as oil, coal, natural gas, and wood [5–7]. Overcoming such problems involves the progress of novel energy storage systems that alleviate environmental pollution, are based on a renewable energy source, and are green and cost effective. To this end, solar cells, supercapacitors, batteries, and capacitors are now commercially available [8–10]. Solar cells, batteries and supercapacitors are the most capable electrical energy storage systems. In supercapacitors, battery type materials are particularly promising because they show outstanding characteristics such as high energy and power densities and good long-term cycling stability; they also do not generate environmental pollution and are inexpensive to fabricate [11–15].

Currently, many researchers are developing various binary and ternary metal oxide/hydroxide/chalcogenide nanostructures [16–20] for use in supercapacitors [21], batteries [22], dye-sensitized solar cells [23], sensors [24], water-splitting [25], hydrogen/oxygen evolution [26,27], and various electronic devices. Among these transition-metal chalcogenides, we have chosen

* Corresponding author. Department of Biological and Environmental Science, College of Life Science and Biotechnology, 6 Dongguk University, 32 Dongguk-ro, Biomedical Campus, Ilsandong-gu, Siksa-dong, 10326, Goyang-si, Gyeonggi-do, South Korea.
E-mail address: sbpkim@dongguk.edu (D.-Y. Kim).

https://doi.org/10.1016/j.electacta.2020.135973
0013-4686/

ternary Mn—Co—chalcogenide nanomaterials for demonstrating their electrochemical energy storage capacities because $MnCo_2S_4$ are having better electrochemical conductivity, nontoxic, readily available, inexpensive, and easy to fabricate. For instance, Zhang et al. [17] effectively produced nanowire-like $MnCo_2S_4$ thin films deposited onto Ti mesh for the O_2 evolution reaction in 1.0 M KOH. They reported that the $MnCo_2S_4$ electrode exhibited good oxygen evolution activity. Jadhav et al. [27] electrodeposited $MnCo_2S_4$ flakes onto a stainless-steel mesh. They reported an oxygen evolution reaction performance as high as 290 mV at a 10 mA cm^{-2}. Wang et al. [28] developed $MnCo_2O_4$@$MnCo_2S_4$ core—shell composite thin films on Ni foam. These $MnCo_2O_4$@$MnCo_2S_4$ thin films for use in asymmetric system was prepared using a hydrothermal techniques. The authors reported that the composite $MnCo_2O_4$@$MnCo_2S_4$ films exhibited a specific capacitance of 1933.3 F g^{-1} at a current density 1 A g^{-1}, respectively. Wang et al. [29] successfully coated $MnCo_2S_4$ nanoparticles with graphene nanosheets for use in asymmetric energy storage system. They concluded that the composites showed superior electrochemical performance.

The literature survey revealed that there are no reports of ternary $MnCo_2S_4$ and halloysite nanocomposites as battery type electrode material. Therefore, ternary $MnCo_2S_4$ materials prepared using a cost-effective and simple coprecipitation method, which was found to be more effective than other physical and chemical methods because it does not require specialized instruments and uses inexpensive chemicals while generating minimal waste. We grew nanoflakes on a nanotube-like nanostructure composite deposited on Ni foam using the screen-printing method. Further the performance of the nanocomposite as an electrode material in a symmetrical energy storage system was investigated in detail. The structural, morphological, compositional, and electrochemical properties of the $MnCo_2S_4$/HNTs composite show that the composite exhibits excellent performance than the individual $MnCo_2S_4$ and HNTs components. This is due to the HNTs coating of the $MnCo_2S_4$ nanoflakes results in a nanoflakes/nanotube $MnCo_2S_4$/HNTs nanocomposite that favors ion transport or ion exchange. The specific capacity values of the composite tested using a three-electrode system was about 359 mAh g^{-1} at 5 mV s^{-1}, which is higher than that of the $MnCo_2S_4$ and HNTs electrodes. The cathode and anode electrodes were prepared using $MnCo_2S_4$/HNTs composite. The electrochemical measurements of the $MnCo_2S_4$/HNTs|| $MnCo_2S_4$/HNTs symmetric system demonstrated good electrochemical performance along with the high charge/discharge capabilities. This system demonstrated an energy density of 6.98 Wh kg^{-1} and power density of 1976.0 W kg^{-1}. The $MnCo_2S_4$/HNTs composite is applicable for symmetric and asymmetric energy storage applications because of its electrical properties.

2. Experimental

2.1. Materials

Analytical grade manganese (II) sulfate hexahydrate ($MnSO_4 \cdot 6H_2O$), cobalt (II) sulfate heptahydrate ($CoSO_4 \cdot 7H_2O$), sodium sulfide ($Na_2S \cdot 5H_2O$), ammonium hydroxide (NH_4OH), and Halloysite (HNTs) nanoclay and polyvinyl alcohol (PVA) from Sigma-Aldrich were used as received. All aqueous solutions in the experiment were prepared by dissolving the corresponding precursors in distilled water.

2.2. Synthesis of $MnCo_2S_4$ thin films

Initially, 100 ml aqueous solutions of 0.1 M $MnSO_4.6H_2O$, 0.1 M $CoSO_4.H_2O$, and 0.2 M $Na_2S.9H_2O$ were prepared separately. At first, the pH of Mn and Co precursors was adjusted to 12 by using aqueous ammonia. These two precursor solutions were gradually mixed. To this mixed solution, a 100 ml solution of 0.2 M Na_2S was added drop wisely. A black-colored precipitate was formed in the alkaline bath and the mixture was stirred for 1 h. The subsequent $MnCo_2S_4$ precipitate was collected by filtration using Whatman grade 1 filter paper and washed with distilled water for several times. The as-synthesized $MnCo_2S_4$ precipitate was annealed at 300 °C for 30 min under Ar atmosphere. The obtained powder was used to fabricate $MnCo_2S_4$ thin films via the screen-printing method.

2.3. Screen printing of $MnCo_2S_4$@HNTs thin films

The powder prepared by a chemical coprecipitation method was used to fabricate thin films of $MnCo_2S_4$, $MnCo_2S_4$/HNTs, and HNTs for electrochemical testing. The required amount of polymer gel was added to the powder to make a sticky paste. After preparation of viscous paste, a uniform and homogenous two layers of $MnCo_2S_4$ thin films were screen printed on Ni foam, air dried overnight for 6 h, and annealed at 200 °C for 1 h to evaporate water content. The mass of active material deposited onto the Ni foam was about 0.9 mg cm^{-2} for all $MnCo_2S_4$, $MnCo_2S_4$/HNTs, and HNTs electrodes.

2.4. Characterization

The crystal structures and phase identification of the powder were recorded using a Rigaku Ultima III diffractometer equipped with a Cu K_α radiation (1.54 Å) source. The nanostructures of the samples were observed by scanning electron microscopy (JEOL JSM-7100) and transmission electron microscopy (HR-TEM; JEOL JEM-2100). X-ray photoelectron spectroscopy (XPS; ULVAC-PHI Quantera SXM) was used to examine the elemental composition of the as-synthesized samples [30,31].

2.5. Electrochemical testing

The electrochemical characteristics were evaluated using as-synthesized $MnCo_2S_4$, $MnCo_2S_4$/HNTs, and HNTs electrodes as a working electrode, Pt as the counter, and Ag/AgCl as reference electrode. The electrode fabrication process is described elsewhere [31,32]. The supercapacitor measurements were performed with the potential range of −0.2 to 0.5 V in the 1 M KOH electrolyte. The cyclic voltammetry (CV), galvanostatic charge-discharge (GCD), and electrochemical impedance spectroscopy (EIS) analysis were performed with an electrochemical workstation (CH Instruments CHI 660E) [32].

2.6. Fabrication of flexible symmetric devices

The flexible symmetric $MnCo_2S_4$/HNTs||$MnCo_2S_4$/HNTs device was assembled as positive and negative electrodes. Both $MnCo_2S_4$/HNTs electrodes were separated using separator, and polymer gel was used as the electrolyte. A similar protocol was applied to prepare polymer gel, which is reported elsewhere [33]. Both $MnCo_2S_4$/HNTs electrodes and the separators are immersed in the polymer gel for 10 s and then natural dried in air for overnight. Finally, both of the electrodes were hard-pressed at 35 °C for 6 h with separator sandwiched together.

3. Results and discussion

3.1. X-ray diffraction (XRD) study

The crystallographic information of the as-synthesized

$MnCo_2S_4$, $MnCo_2S_4$/HNTs composite, and HNTs powders were attained with XRD analysis. Fig. 1A shows the XRD patterns of the $MnCo_2S_4$, $MnCo_2S_4$/HNTs composite, and HNTs samples. The diffraction peaks of the $MnCo_2S_4$ and HNTs appeared at 19.86°, 35.42°, 38.40°, 54.84°, 62.59°, 73.84° and at 12.81°, 19.86°, 24.36°, 35.42°, 38.40°, 54.84°, and 62.59°, respectively; these peaks can be assigned to the corresponding planes (111), (311), (222), (422), (440), (620) and (001), (100), (002), (110), (003), (210), (300) of the cubic and hexagonal structures, respectively [27,29]. The XRD patterns of the $MnCo_2S_4$ and HNTs are well matched standard JCPDS card nos. 023−1237, 19−0366, and 029−1487, respectively. Fig. 1Ab shows the XRD patterns of composite samples a and c. The XRD pattern of sample b displays all the diffraction peaks observed in the patterns of samples a and c, demonstrating that the composite of the $MnCo_2S_4$ and HNTs powders was uniformly mixed, resulting in a pure phase of the $MnCo_2S_4$/HNTs composite. The XRD pattern does not show any peak other phase in the composite. Fig. 1Ab confirms the XRD pattern of the $MnCo_2S_4$/HNT composite; the diffraction peaks corresponding to crystal planes (001), (111/100), (111/002), (211), (311/110), (222/003), (422/210), (440/300), and (620/613) are observed at 12.81°, 19.86°, 24.36°, 26.63°, 35.42°, 38.40°, 54.84°, 62.59°, and 73.84°, respectively [30]. All the diffraction peaks indicate that the compound is composed with a hybrid phases of the hexagonal/cubic crystal structures. The pattern of the composite shows stronger and sharper diffraction peaks than the patterns of the other samples, indicating that the composite sample is more crystalline than the other phases, without any impurities [31]. XRD analyses revealed the formation of homogeneous composites of $MnCo_2S_4$ and HNTs materials. From the XRD results, we conclude that the $MnCo_2S_4$ and HNTs materials were successfully amalgamated into a composite. These results indicate that the $MnCo_2S_4$, $MnCo_2S_4$/HNTs, and HNTs were successfully grounded into powders after being coprecipitated [32].

3.2. X-ray photoelectron spectroscopy (XPS) study

XPS techniques was used to confirm the elemental composition of the as-synthesized $MnCo_2S_4$, $MnCo_2S_4$/HNTs, and HNTs. Fig. 1B (a−c) indications the survey spectra of $MnCo_2S_4$, $MnCo_2S_4$/HNTs, and HNTs samples, respectively. Fig. 1Ba shows that Mn, Co, and S elements are present in the samples. Similarly, Al, Si, and O elements are observed in Fig. 1Bc. The survey spectrum of the $MnCo_2S_4$/HNTs composite samples confirms the presence of all the elements already observed in the $MnCo_2S_4$ and HNTs samples. The survey spectrum of the $MnCo_2S_4$/HNTs composite shows no other chemical valence or elemental states on the surface of the $MnCo_2S_4$/HNTs composite, demonstrating that the as-synthesized composite is comparatively pure than the other two samples. Fig. 1C reveals the Mn 2p core levels of the $MnCo_2S_4$/HNTs composite; two peaks are observed at the binding energies 659.07 and

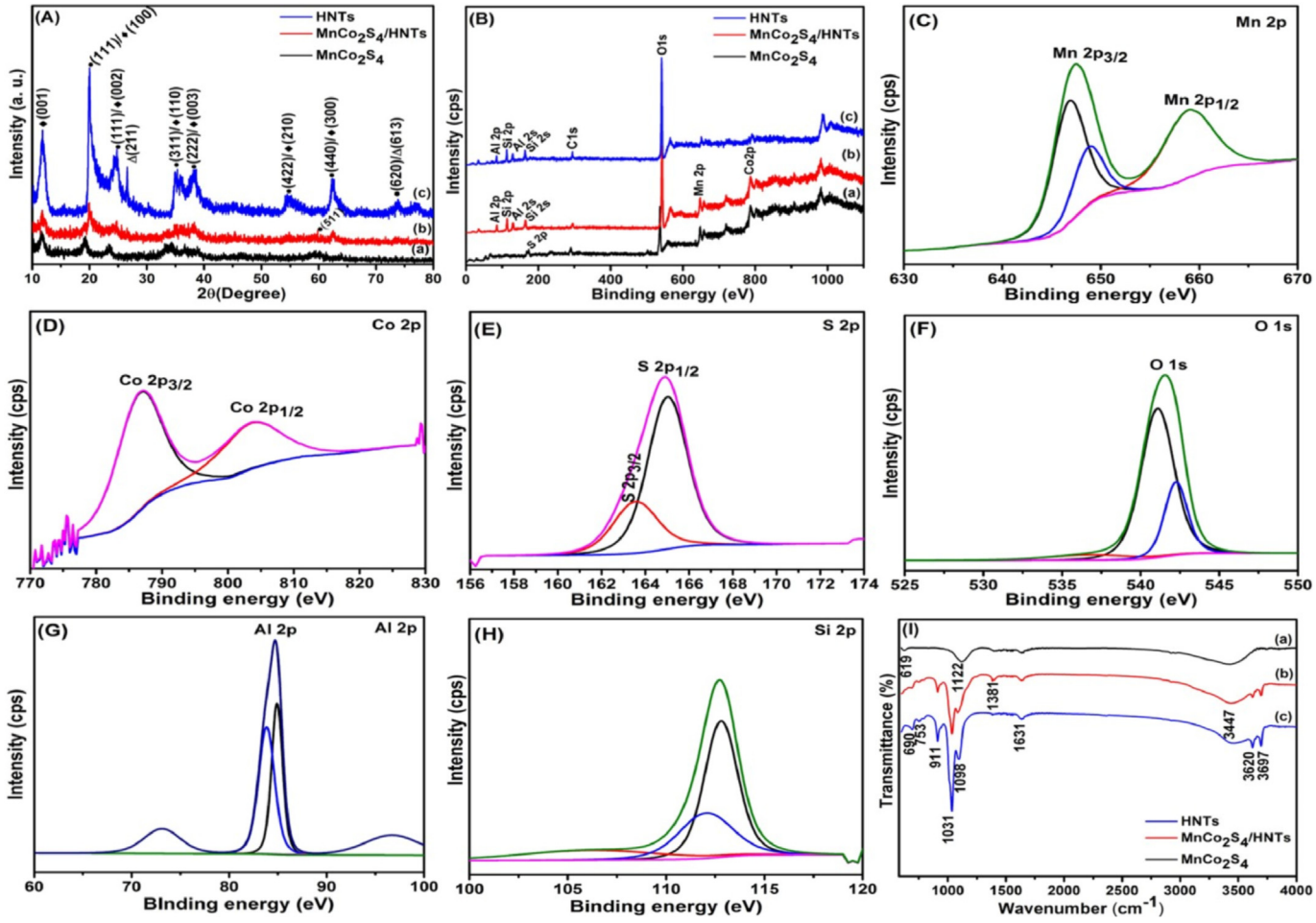

Fig. 1. (A) XRD patterns of $MnCo_2S_4$, $MnCo_2S_4$/HNTs composite, HNTs, respectively, (B) XPS survey spectra of $MnCo_2S_4$, $MnCo_2S_4$/HNTs composite, HNTs, respectively, (C−H) High resolution spectra of Mn 2p, Co 2p, S 2p, O 1s, Al 2p, and Si 2p of $MnCo_2S_4$/HNTs composite sample, respectively. (I) FT-IR spectra of $MnCo_2S_4$, $MnCo_2S_4$/HNTs composite, HNTs samples.

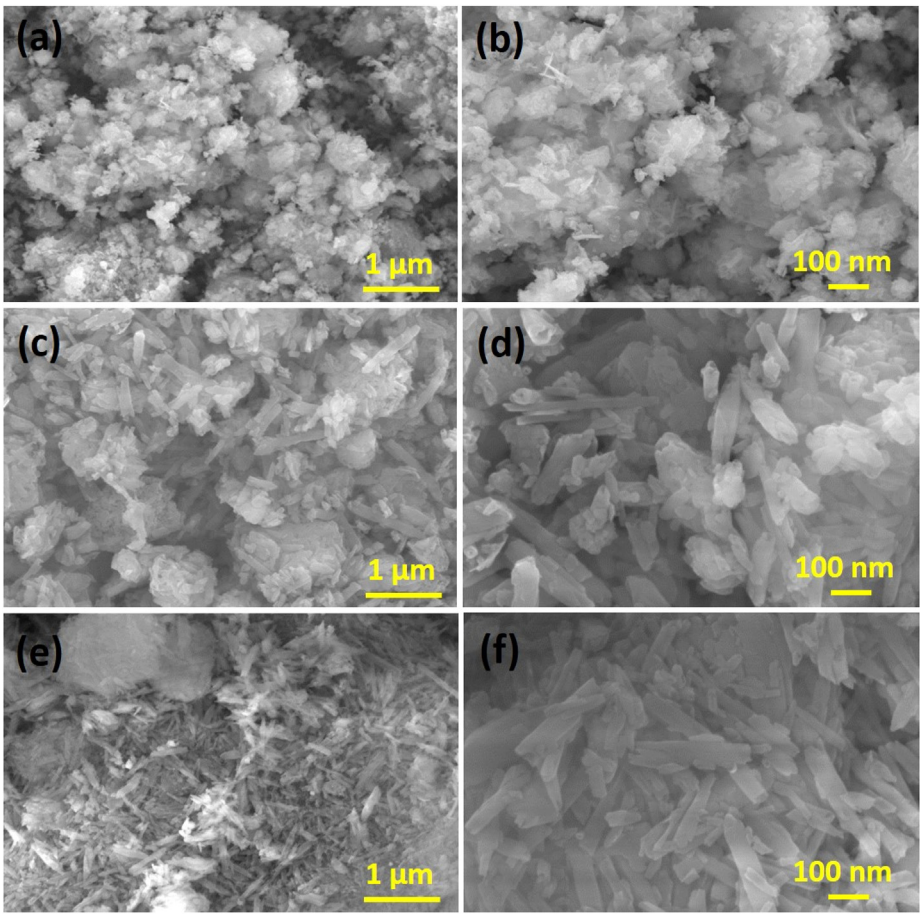

Fig. 2. **(a–f)** SEM images of $MnCo_2S_4$, $MnCo_2S_4$/HNTs composite, and HNTs samples with different magnification, respectively.

647.46 eV assigned to the Mn $2p_{1/2}$ and Mn $2p_{3/2}$ states, respectively; the energy difference between the Mn $2p_{1/2}$ and Mn $2p_{3/2}$ states is about 11.61 eV, which indicate that Mn exists in the Mn^{2+} state. Fig. 1D shows the Co 2p core levels of the $MnCo_2S_4$/HNTs composite. The two peaks observed at binding energies of 786.80 and 804.41 eV are due to the Co $2p_{3/2}$ and Co $2p_{3/2}$ states, respectively [28–33]. The difference in binding energy between the Co $2p_{3/2}$ and Co $2p_{1/2}$ states is about 17.61 eV, confirming the presence of both Co^{2+} and Co^{3+} [16]. Fig. 1E displays the S 2p high resolution of the $MnCo_2S_4$/HNTs composite. The spectrum shows two strong peaks at binding energies of 164.86 and 163.49 eV, which related to the S $2p_{1/2}$ and S $2p_{3/2}$ states, respectively [29]. In Fig. 1F, peaks of O 1s are observed because the sample was prepared under an air atmosphere. Fig. 1(G and H) appearances the high-resolution spectrum of Al 2p and Si 2p, with corresponding binding energies of 84.79 and 112.71 eV, respectively. The fitted C 1s high-resolution spectrum of the $MnCo_2S_4$/HNTs composite reveals a peak at 284.1 eV for C 1s, which is associated to a C–Si species [34]. From these results confirmed that Mn 2p, Co 2p, O 1s, S 2p, Al 2p, and Si 2p elements are present on the surface of the $MnCo_2S_4$/HNTs composite.

3.3. FT-IR study

Fig. 1I shows the FT-IR spectra of the $MnCo_2S_4$, $MnCo_2S_4$/HNTs, and HNTs samples. The spectrum of the $MnCo_2S_4$ shows a peak at 3447 cm^{-1} that is ascribed to the O–H stretching vibration mode [35]. The strong absorption peaks at 1122 cm^{-1} are attributed to a stretching vibration mode of C–OH groups, whereas the two peaks at 1381 and 1122 cm^{-1} are assigned to C–O and O–H stretching vibrations, respectively [36]. The main absorption peak at 619 cm^{-1}, confirmed the stretching vibrations of Mn–O and Co–S bonds [37,38], demonstrate the formation of Mn–Co–S compounds [35–39]. For the HNTs, the peaks at 3620 and 3697 cm^{-1} are corresponding to O–H stretching vibration modes [40]. The vibrational peak at 1631 cm^{-1} is assigned to an O–H stretching mode [38], which arises from water in the samples. The strong peaks at 1031 and 1098 cm^{-1} are related to the stretching vibration modes of the Si–O network [24]. The peaks at 911, 753, and 690 cm^{-1} are related to O–H, Al–O–Si, and Si–O–Si groups [41], respectively. The spectrum of the $MnCo_2S_4$/HNTs composite shows all the absorption peaks observed in the spectra of the $MnCo_2S_4$ and the HNTs, confirming that the stretching vibration modes of both phases are present. Thus, the FT-IR analysis indicates that the $MnCo_2S_4$/HNTs composite formed without any other impurities.

3.4. SEM study

Fig. 2(a–f) displays the SEM micro images of the $MnCo_2S_4$, $MnCo_2S_4$/HNTs composite, and HNTs at different magnifications. Fig. 2(a and b) shows SEM images of $MnCo_2S_4$ samples prepared using the coprecipitation method. The SEM images of the $MnCo_2S_4$ samples show that porous nanoflakes with irregular growth fully covered their surface. The higher-magnification image (Fig. 2b) shows numerous porous-interconnected nanoflakes with various thicknesses and size. The average thickness of the nanoflakes

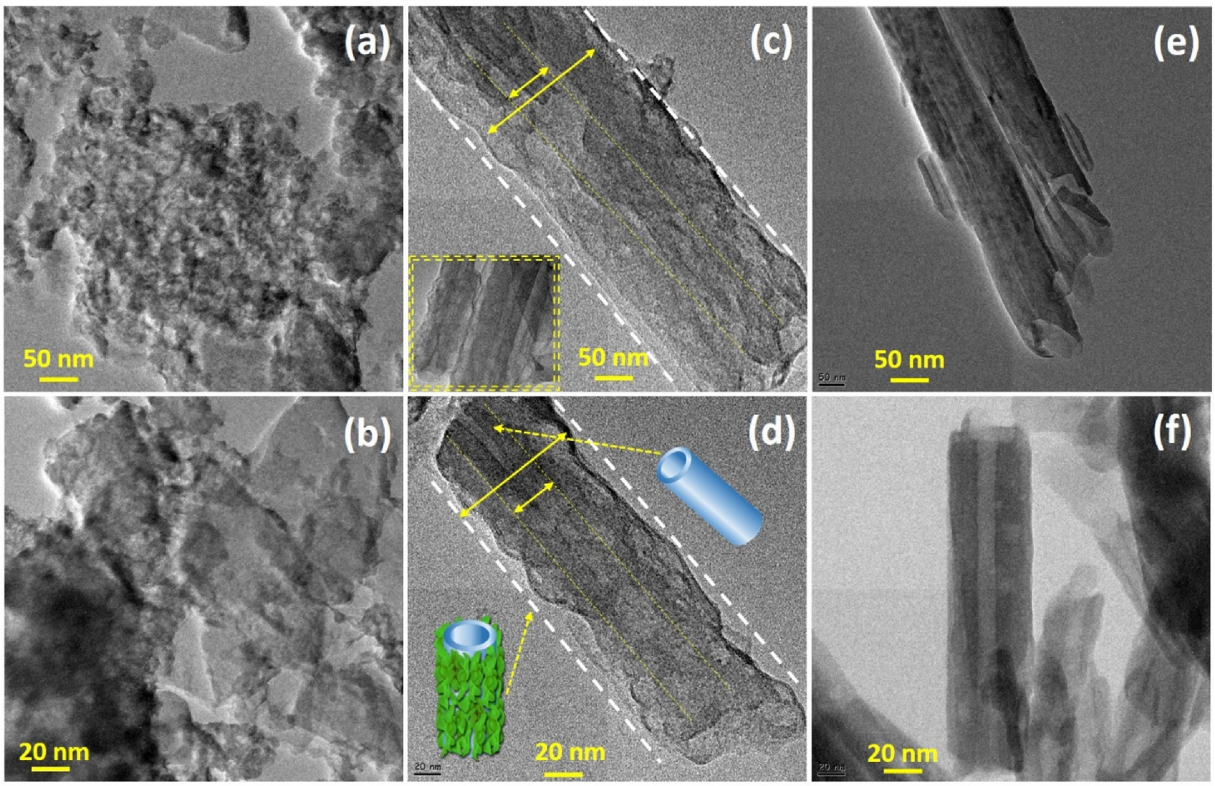

Fig. 3. (a–f) TEM images of $MnCo_2S_4$, $MnCo_2S_4$/HNTs composite, and HNTs samples with different magnification, respectively.

ranges between 300 and 400 nm. Fig. 2(e and f) shows SEM images of halloysite at different magnifications. These SEM images shows cylindrical nanotubes with different lengths and diameters. The average length and diameter of the nanotubes are approximately 400–500 nm and 50–100 nm, respectively. These SEM images were well matched with the previously reported SEM images of halloysite nanotubes [42,43]. Fig. 2(c and d) also shows SEM images of the $MnCo_2S_4$/HNTs composite sample. The images at higher magnification show that the porous nanoflakes resemble fully re-capped nanostructures on nanotubes [44]. Fig. 2d reveals that all the nanoflakes are fully decorated on the HNTs nanotubes. The outer layer of surface exhibits a greater porosity than the neat $MnCo_2S_4$ and HNTs samples; this type of composite sample favors easy ion transport during the electrochemical reactions [45]. In the present work, we focused on hollow cylindrical nanostructures because hollow tube-like nanostructures enable faster ion and mass transfer. The SEM analysis confirmed that the $MnCo_2S_4$/HNTs samples provided greater porosity and a larger active surface area than both the $MnCo_2S_4$ and HNTs samples [46].

Fig. 3(a–f) shows TEM images of the $MnCo_2S_4$, $MnCo_2S_4$/HNTs composite, and HNTs with different magnifications. Fig. 3(a and b) presents TEM images of $MnCo_2S_4$, indicating that the sample consists of porous interconnected nanoflakes-like nanostructures. Fig. 3(c and d) shows TEM images of the $MnCo_2S_4$/HNTs composite. The TEM images of the composite clearly show that the nanoflakes are fully and uniformed coated on the nanotubes and that the morphology of the composite samples (Fig. 3(e and f)). The thickness and diameters increased after the $MnCo_2S_4$/HNTs composite was formed and all the nanotubes are fully coated with $MnCo_2S_4$ nanoflakes. These TEM images demonstrate that the nanoflakes well cover the HNTs. The composite might be useful as an electrode material for electrical energy storage systems due to its morphology which can provide a larger reactive area and enables the fast motion of electrons [47].

3.5. Electrochemical properties of electrodes

Fig. 4a displays the CV curves of the $MnCo_2S_4$, $MnCo_2S_4$/HNTs, and HNTs electrodes in the potential range of −0.2 and 0.5 V at a scan rate of 100 mV s^{-1} in a 1 M KOH electrolyte. The CV curve in Fig. 4a shows that the $MnCo_2S_4$/HNTs composite electrode reveals the largest surface area and highest current density (200 mA cm^{-2}) among the investigated electrodes; thus, the $MnCo_2S_4$/HNTs electrode reveals a higher specific capacity than the $MnCo_2S_4$ and HNTs electrodes. Similar results are observed in the GCD curves of the $MnCo_2S_4$, $MnCo_2S_4$/HNTs, and HNTs electrodes recorded range from −0.2 to 0.5 V at a constant current density of 7 mA cm^{-2} in 1 M KOH electrolyte (Fig. 4c). The GCD results indicates that the $MnCo_2S_4$/HNTs sample exhibits the longest charge–discharge time among the three electrode materials, indicating that the composite electrode provides the greatest specific capacities. Fig. 4 (b, d) shows the current and charge–discharge times for the different electrodes. It can be seen From Fig. 4 (b, d), that the composite electrode was superior to the other two $MnCo_2S_4$ and HNTs electrodes. We therefore used the composite electrode in further electrochemical studies and symmetric device fabrication [48].

Fig. 5a and S1 (a, b) displays the CV curves of the $MnCo_2S_4$/HNTs composite, $MnCo_2S_4$, and HNTs electrodes at various scan rates from the 5–100 mV s^{-1} in 1 M KOH and scanned over the potential range from −0.2 to 0.5 V, respectively. The CV curves show that the redox and oxidation peaks move in the positive and negative directions, respectively, as the scan rate is increased from 5 to 100 mV s^{-1} and that the shifts are reversible when the scan rate is decreased. Fig. 5b shows the specific capacities at different scan rates for the $MnCo_2S_4$, $MnCo_2S_4$/HNTs, and HNTs electrodes. Among these electrodes, the $MnCo_2S_4$/HNTs shows higher values of specific

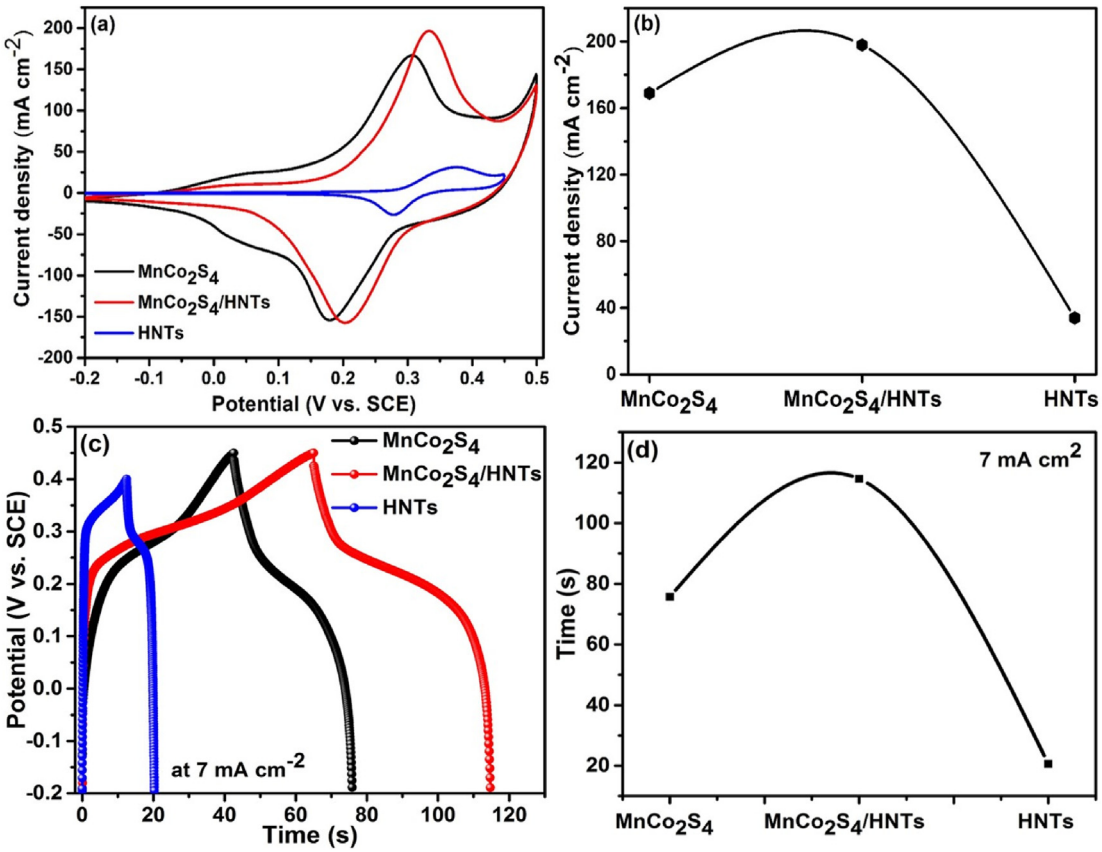

Fig. 4. (a) CV curves of $MnCo_2S_4$, $MnCo_2S_4$/HNTs composite and HNTs electrodes at a 100 mV s^{-1} in the potential range −0.2 to 0.5 V, respectively (b) Current density of $MnCo_2S_4$, $MnCo_2S_4$/HNTs composite, and HNTs electrodes at a 100 mV s^{-1}, (c) Galvanostatic charge discharge curve of $MnCo_2S_4$, $MnCo_2S_4$/HNTs composite and HNTs electrodes at a 7 mA cm^{-2} in 1 M KOH electrolyte, (d) Discharge time of $MnCo_2S_4$, $MnCo_2S_4$/HNTs composite, and HNTs electrodes at a 7 mA cm^{-2} in a 1 M KOH electrolyte.

capacities than the other two electrodes at different scan rate between 5 and 100 mV s^{-1}. These values show that the $MnCo_2S_4$/HNTs electrode exhibits greater specific capacities than the other two electrodes, which is attributed to the porous surface and hall reactive surface area of the nanoflakes/nanotube-like hierarchical nanostructure [18,49]. This nanostructure enables fast ionic motion and ion transfer during the electrochemical measurements [18–21].

Fig. 5c and S1 (c, d) indications the GCD curves of the $MnCo_2S_4$/HNTs, $MnCo_2S_4$, and HNTs electrodes at various current densities from 2 to 7 mA cm^{-2} in the potential range from −0.2 to 0.5 V in 1 M KOH. The results show that the GCD curves are nonlinear in nature, indicating that a fast faradaic redox reaction occur at the interface between electrode and the electrolyte. The specific capacities values of the $MnCo_2S_4$/HNTs, $MnCo_2S_4$, and HNTs electrodes were calculated using the standard relation (1),

$$\text{Specific capacity} = (I \times \Delta t)/m \quad (1)$$

where *I* is the charging/discharging current density (mA), Δ*t* is the discharge time (h), and *m* is the active mass of the electrode (g). Fig. 5d shows the specific charge capacities from GCD curves with the different current densities. The obtained specific capacities were 258, 302 and 29 mAh g^{-1} for the $MnCo_2S_4$, $MnCo_2S_4$/HNTs, and HNTs electrodes, respectively. Thus, the $MnCo_2S_4$/HNTs electrode exhibits better electrochemical performance than the pure $MnCo_2S_4$ and HNTs electrodes at a current density of 2 mA cm^{-2}. The calculated specific capacities for the $MnCo_2S_4$/HNTs electrodes were 302, 260, 249, 237, and 229 mAh g^{-1} at current densities of 2, 4, 5, 6, and 7 mA cm^{-2}, respectively. The maximum specific capacity in the present case is highly appreciable as compared to previously reported $MnCo_2S_4$-based electrodes in Table 1. For example, Elshahawy et al. [16] hydrothermally synthesized $MnCo_2S_4$ thin films for supercapacitors. They reported a specific capacity of 175 mAh g^{-1} (1402 F g^{-1}) at 1 A g^{-1}, with 95% capacitance retention and good cycling stability. Liu et al. [50] prepared $MnCo_2S_4$ hydrothermally for use in supercapacitors and calculated a substantial specific capacity of approximately 287 mAh g^{-1} (2067 F g^{-1}) at a 1 A g^{-1} current density. They also fabricated an asymmetric supercapacitor using $MnCo_2S_4$ and RGO materials. Fig. 5e demonstrates the cycling stability of the $MnCo_2S_4$/HNTs electrode with potential range from −0.2 to 0.5 V in a 1 M KOH electrolyte at a scan rate of 100 mV s^{-1}. The superb specific capacity retention after cycling may be due to the influences of the extremely porous surface of the nanowire-like nanostructure of the composite electrodes.

To further characterize the as-prepared electrode materials, we performed EIS analyses. Fig. 5f shows the Nyquist plots of the $MnCo_2S_4$, $MnCo_2S_4$/HNTs, and HNTs electrodes in the frequency range 1–100 kHz; the inset of the figure shows the equivalent circuit and high resolution of Nyquist plots [51]. The values of the solution resistance (R_s) are 1.19, 0.89, and 1.10 Ω for the $MnCo_2S_4$, $MnCo_2S_4$/HNTs, and HNTs electrodes, respectively; charge transfer resistance (R_{ct}) values are 1.20, 0.91, and 1.25 Ω for the $MnCo_2S_4$, $MnCo_2S_4$/HNTs, and HNTs electrodes, respectively. These values of the R_s and R_{ct} demonstrate that the $MnCo_2S_4$/HNTs electrode exhibits a lower resistance than the other electrodes. Thus, the $MnCo_2S_4$/HNTs electrode exhibits higher conductivity than the

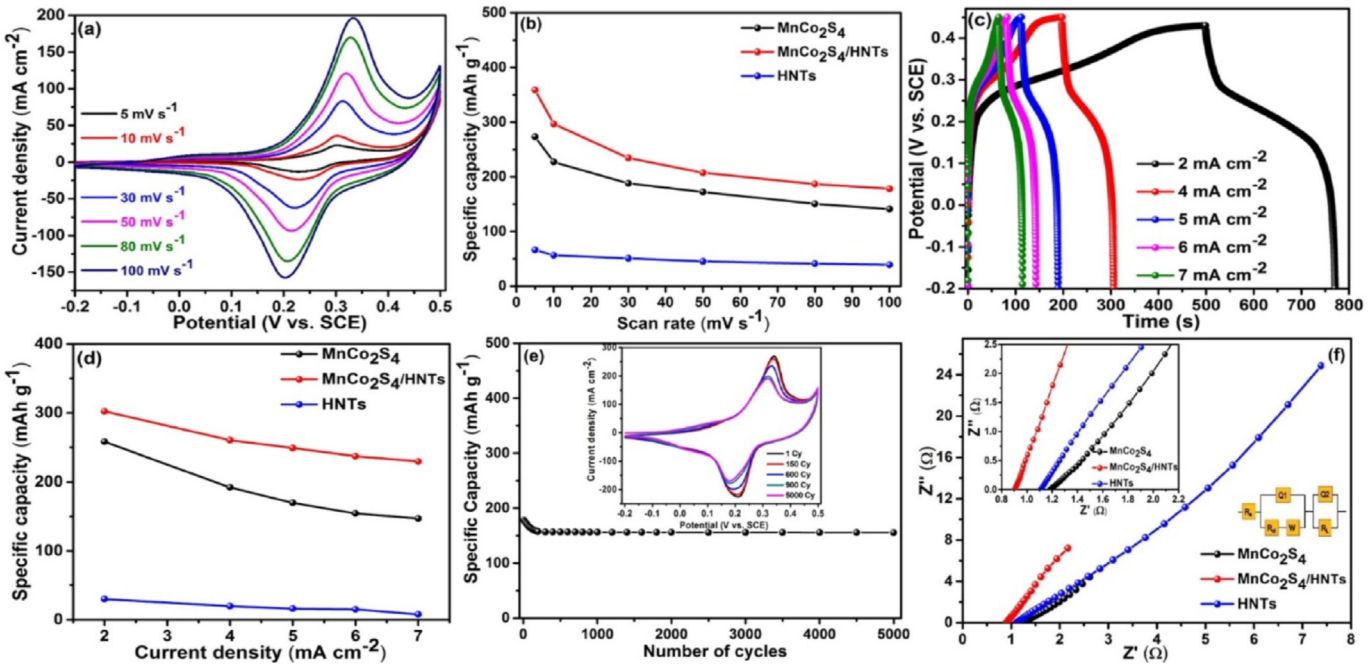

Fig. 5. (a) CV curves of the $MnCo_2S_4$/HNTs composite at a different scan rate from 5 to 100 mV s^{-1} in the potential range −0.2 to 0.5 with 1 M KOH electrolytes, (b) Specific capacities of the $MnCo_2S_4$, $MnCo_2S_4$/HNTs composite and HNTs electrodes with different scan rates from 5 to 100 mV s^{-1} in the potential range −0.2 to 0.5 V with 1 M KOH electrolytes, respectively, (c) CD curves of the $MnCo_2S_4$/HNTs composite at a different current densities from 2 to 7 mA cm^{-2} in the potential range −0.2 to 0.5 V, (d) Specific capacities of the $MnCo_2S_4$, $MnCo_2S_4$/HNTs composite and HNTs electrodes with respect to the different current densities, (e) Cycling stability of the $MnCo_2S_4$/HNTs composite with various cycle at 100 mV s^{-1} scan rate, inset shows the CV curves of different cycles, (f) Nyquist plots of $MnCo_2S_4$, $MnCo_2S_4$/HNTs composite, HNTs electrodes, inset shows the high resolution images and equivalent circuit.

Table 1
Comparison of the specific capacity of *$MnCo_2S_4$/HNTs* electrode with different forms from previous reports.

Materials	Method	Current density/ Scan rate	Potential (V)	Specific capacitance (F g^{-1})	Specific capacity (mAh g^{-1})	Energy density (Wh kg^{-1})	Power density (W kg^{-1})	Reference
$MnCo_2S_4/CoS_{1.097}$	Reflux	1 A g^{-1}	0.0–0.6	1006	167.66	51.6	800	[15]
$MnCo_2S_4$	Hydrothermal	1 A g^{-1}	0.0–0.6	1402	233.66	16.2	–	[16]
$NiCo_2S_4$	Hydrothermal	4 A g^{-1}	−0.4–0.4	777	172.6	17.1	2250	[19]
$MnCo_2S_4$	Solvothermal	1 A g^{-1}	0.0–0.4	4730	525.7	15.2	–	[21]
CoS_2/MoS_2	Hydrothermal	5 mV s^{-1}	0.0–0.5	406	56.38	–	–	[26]
$MnCo_2O_4/MnCo_2S_4$	Hydrothermal	4 A g^{-1}	0.0–0.5	1933	268.47	50.75°	1260	[28]
$MnCo_2S_4$	Sulfurization	1 A g^{-1}	0.0–0.6	1324	220.60	28.0	1800	[29]
$NiCo_2S_4$	SILAR	5 mV s-1	−0.2–0.6	1076	239.11	–	–	[44]
$MnCo_2S_4$	Hydrothermal	1 A g^{-1}	−0.1–0.4	2067	287.	31.3	800	[50]
Ni–CO–S	Electrodeposition	5 A g^{-1}	−0.2–0.6	1418	315.11	60	1800	[52]
NiS/MoS_2/CNT// activated carbon	Hydrothermal	0.5 A g^{-1}	0.0–0.5	757	105.13	40	–	[54]
NiS	Sulfuration	1 A g^{-1}	−0.1–0.6	1122	218.16	31	900	[55]
$NiCo_2S_4@Ni_3S_2$	Hydrothermal and electrodeposition	0.5 A g^{-1}	0–0.6	272	45.44	32.75	361	[56]
$MnCo_2S_4$/HNTs	*Screen printing*	5 mV s^{-1}	*−0.2–0.6*	*1846*	*359*	*6.98*	*1976*	Present study

other two electrodes because of its porous nanostructure, which similarly affected the electrochemical performance [52]. Thus, the $MnCo_2S_4$/HNTs electrode was used in the subsequent symmetric electrochemical energy storage investigation.

3.5.1. *$MnCo_2S_4$/HNTs||$MnCo_2S_4$/HNTs symmetric electrode*

To demonstrate the practical application of the composite electrode in an electrochemical energy storage, we fabricated symmetric device using $MnCo_2S_4$/HNTs electrodes as working positive and negative electrodes [53]. The electrochemical performance and cycling stability were estimated by CV, GCD, and EIS [54]. Fig. S2 shows a schematic of the device fabrication of the symmetric device. Fig. 6a shows the results of the electrochemical measurements of the symmetric $MnCo_2S_4$/HNTs||$MnCo_2S_4$/HNTs electrode in the potential range 0.0–0.8 V, at various scan rates. The cyclic voltammograms show that the maximum current density around 2.5 mA cm^{-2} at a 100 mV s^{-1} scan rate. The specific capacities values calculated from the CV curves decrease with increasing scan rate from 10 to 100 mV s^{-1}, as shown in Fig. 6b. The GCD curves of the $MnCo_2S_4$/HNTs||$MnCo_2S_4$/HNTs symmetric device at various current densities from 5 to 10 mA cm^{-2}, which confirms that the symmetric device exhibits high supercapacitor performance and that its charge and discharge curves exhibit a mirror-image relationship [55]. This typical battery type behavior indicated by the charge–discharge curves may involve a faradaic redox reaction. The calculated specific capacities are 76.12, 52.5,

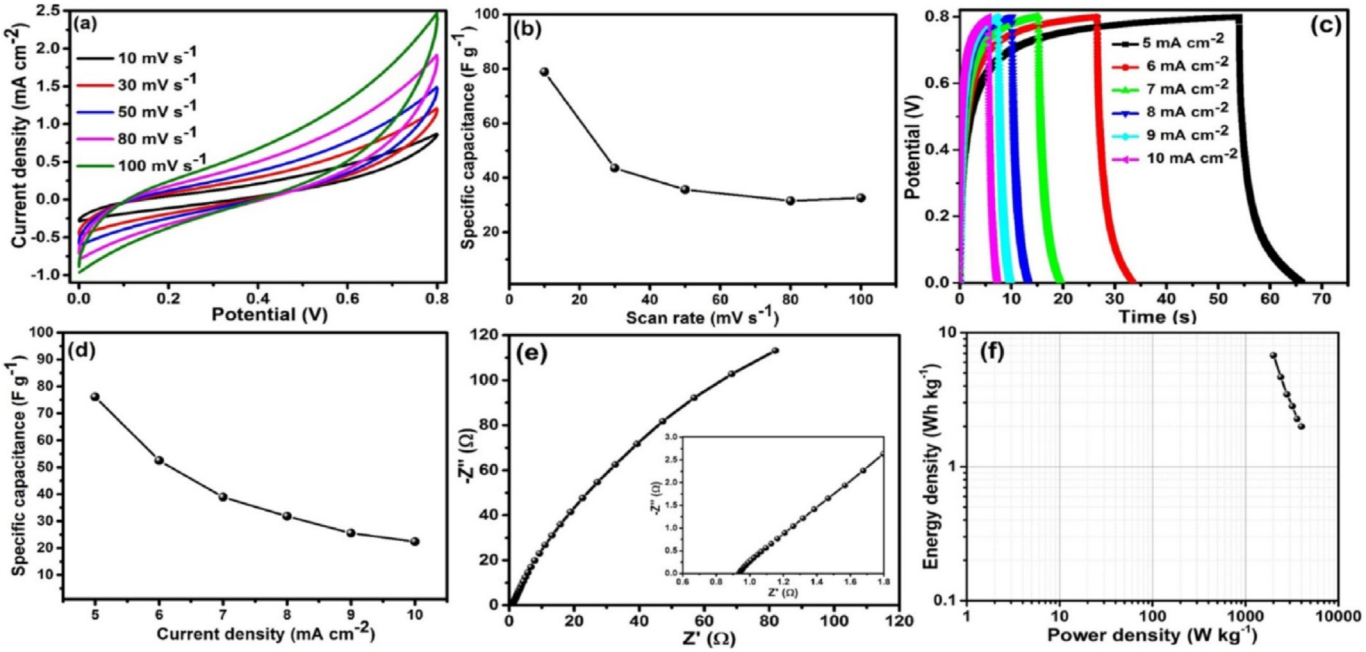

Fig. 6. (a) CV curves of symmetric supercapacitor (SC) at various scan rate from 10 to 100 mV s^{-1}, (b) Specific capacitance with respect to the different scan rates of the symmetric supercapacitor, (c) Charge-discharge curves at various current densities, (d) Specific capacitance with respect to the different current densities from 5 to 10 mA cm^{-2} in the positive window 0−0.8 V, (e) Nyquist plots of the symmetric SC, (f) Ragone plot of the SC device.

38.93, 31.86, 25.36 and 22.37 F g^{-1} at different current densities from 5 to 10 mA cm^{-2}, as shown in Fig. 6d. Nyquist plots show the prepared symmetric SC is more conductive as shown in Fig. 6e. After the electrochemical measurements, we calculated the specific energy (E) and specific power (P) of the $MnCo_2S_4$/HNTs symmetric system; the results are shown in Ragone plots (Fig. 6f). The specific energy is 6.98 Wh kg^{-1}, and the specific power is 19676.0 W kg^{-1}. These values show that the $MnCo_2S_4$/HNTs symmetric system provides higher specific energy and power than previously reported $MnCo_2S_4$-based devices [56].

4. Conclusions

In this report, the $MnCo_2S_4$, HNTs, and $MnCo_2S_4$/HNTs composites were synthesized using a two-step process that includes coprecipitation followed by screen printing. The obtained $MnCo_2S_4$/HNTs nanoflakes composite covered on the core nanotubes-like nanostructures exhibit remarkably better electrochemical performance than the $MnCo_2S_4$ and HNTs alone. The $MnCo_2S_4$/HNTs composite samples exhibited outstanding values of a specific capacities of 359 mAh g^{-1} at a scan rate 5 mV s^{-1} in 1 M KOH electrolyte. The electrochemical properties of the symmetric system include good electrical conductivity. Furthermore, the SC device assembled using positive and negative electrodes of $MnCo_2S_4$/HNTs||$MnCo_2S_4$/HNTs exhibited a specific capacity of 76 F g^{-1} and an outstanding energy density of 6.98 Wh kg^{-1} at a power density of 1976.0 W kg^{-1}. Thus, the results show that the $MnCo_2S_4$/HNTs||$MnCo_2S_4$/HNTs cell is a capable and attractive electronic device for symmetric electrochemical energy storage applications. We conclude that the $MnCo_2S_4$/HNTs electrode with enhanced cell performance has strong potential for use in various asymmetric energy storage devices.

Author statement

S.K.S. design the experiment scheme, S.K.S. MBJ, and N.C.M. carried out the experiments. All authors, S.K.S., G.S.G., C.B., D.-Y.K., A.D.J., A.A.K., N.C.M., and C.B., S.R., involved to the characterization of the electrode and the discussions prominent up to the writing of the manuscript. S.K.S. and D.-Y.K. discussed main part and that led to the final manuscript; all authors read and approved manuscript.

Declaration of competing interest

The authors declare that they have no known competing financial interests or personal relationships that could have appeared to influence the work reported in this paper.

Acknowledgment

Analysis of samples was supported by Dongguk University, Seoul, Korea Research Fund 2018. ADJ is thankful to DST, Govt. of India for financial assistance under the DST INSPIRE Faculty Scheme [DST/INSPIRE/04/2017/002737].

Appendix A. Supplementary data

Supplementary data to this article can be found online at https://doi.org/10.1016/j.electacta.2020.135973.

References

[1] B.E. Conway, Electrochemical Capacitors: Scientific Fundamentals and Technology Applications, Kluwer Academic/Plenum Publishers, New-York, 1999.
[2] T. Brousse, D. Belanger, J.W. Long, To Be or not to Be pseudocapacitive? J. Electrochem. Soc. 162 (2015) A5185−A5189.
[3] Y.J. Wang, D.P. Wilkinson, J. Zhang, Noncarbon support materials for polymer electrolyte membrane fuel cell electrocatalysts, Chem. Rev. 111 (2011) 7625−7651.
[4] Y. Zhai, Y. Dou, D. Zhao, P.F. Fulvio, R.T. Mayes, S. Dai, Carbon materials for chemical capacitive energy storage, Adv. Mater. 23 (2011) 4828−4850.
[5] Y. Shao, M.F. El-Kady, L.J. Wang, Q. Zhang, Y. Li, H. Wang, M.F. Mousaviae, R.B. Kaner, Graphene-based materials for flexible supercapacitors, Chem. Soc. Rev. 44 (2015) 3639−3665.

[6] Y. Zhu, X. Ji, C. Pan, Q. Sun, W. Song, L. Fang, Q. Chen, C.E. Banks, A carbon quantum dot decorated RuO_2 network: outstanding supercapacitances under ultrafast charge and discharge, Energy Environ. Sci. 6 (2013) 3665–3675.

[7] Y. Wang, Y. Song, Y. Xia, Electrochemical capacitors: mechanism, materials, systems, characterization and applications, Chem. Soc. Rev. 45 (2016) 5925–5950.

[8] R. Jin, Y. Cui, S. Gao, S. Zhang, L. Yang, G. Li, CNTs@NC@$CuCo_2S_4$ nanocomposites: an advanced electrode for high performance lithium-ion batteries and supercapacitors, Electrochim. Acta 273 (2018) 43–52.

[9] R. Gao, Q. Zhang, F. Soyekwo, C. Lin, R. Lv, Y. Qu, M. Chen, A. Zhu, Q. Liu, Novel amorphous nickel sulfide@CoS double-shelled polyhedral nanocages for supercapacitor electrode materials with superior electrochemical properties, Electrochim. Acta 237 (2017) 94–101.

[10] A. Sun, L. Xie, D. Wang, Z. Wu, Enhanced energy storage performance from Co-decorated MoS_2 nanosheets as supercapacitor electrode materials, Ceram. Int. 44 (2018) 13434–13438.

[11] Z. Wang, X. Li, Y. Yang, Y. Cui, H. Pan, Z. Wang, B. Chen, G. Qian, Highly dispersed b-NiS nanoparticles in porous carbon matrices by a template metal-organic framework method for lithium-ion cathode, J. Mater. Chem. A. 2 (2014) 7912–7916.

[12] J. Zhang, H. Guan, Y. Liu, Y. Zhao, B. Zhang, Hierarchical polypyrrole nanotubes@$NiCo_2S_4$ nanosheets core-shell composites with improved electrochemical performance as supercapacitors, Electrochim. Acta 258 (2017) 182–191.

[13] H. Jia, Y. Song, J. Wu, W. Fu, J. Zhao, X. Liu, A novel P-doped $MnCo_2S_4$ nanoneedles assembled dandelion-like structure for high performance hybrid supercapacitors, Mater. Lett. 233 (2018) 55–58.

[14] B.Y. Guan, L. Yu, X. Wang, S. Song, X.W. Lou, Formation of onion-like $NiCo_2S_4$ particles via sequential ion-exchange for hybrid supercapacitors, Adv. Mater. 29 (2017) 1605051–1605055.

[15] X. Yu, J. Yu, L. Hou, A. Gagnoud, Y. Fautrelle, Z. Ren, X. Li, Double-shelled hollow hetero-$MnCo_2S_4/CoS_{1.097}$ spheres with carbon coating for advanced supercapacitors, J. Power Sources 408 (2018) 65–73.

[16] A.M. Elshahawy, X. Li, H. Zhang, Y. Hu, K.H. Ho, C. Guan, J. Wang, Controllable $MnCo_2S_4$ nanostructures for high performance hybrid supercapacitors, J. Mater. Chem. A 5 (2017) 7494–7506.

[17] X. Zhang, C. Si, X. Guo, R. Kong, F. Qu, A $MnCo_2S_4$ nanowire array as an earth-abundant electrocatalyst for an efficient oxygen evolution reaction under alkaline conditions, J. Mater. Chem. A 5 (2017) 17211–17215.

[18] G. Liu, B. Wang, L. Wang, T. Liu, T. Gao, D. Wang, Facile controlled synthesis of a hierarchical porous nanocoral-like Co_3S_4 electrode for high performance supercapacitors, RSC Adv. 6 (2016) 54076–54086.

[19] L. Hou, H. Hua, R. Bao, Z. Chen, C. Yang, S. Zhu, G. Pang, L. Tong, C. Yuan, X. Zhang, Anion-exchange formation of hollow $NiCo_2S_4$ nanoboxes from mesocrystalline nickel cobalt carbonate nanocubes towards enhanced pseudocapacitive properties, Chem. Plus. Chem. 81 (2016) 557–563.

[20] Z. Li, X. Li, L. Xiang, X. Xie, X. Li, D.R. Xiao, J. Shen, W. Lu, L. Lu, S. Liu, Three-dimensional hierarchical nickel–cobalt–sulfide nanostructures for high performance electrochemical energy storage electrodes, J. Mater. Chem. A 4 (2016) 18335–18341.

[21] A. Pramanik, S. Maiti, M. Sreemany, S. Mahanty, Carbon doped $MnCo_2S_4$ microcubes grown on Ni foam as high energy density faradaic electrode, Electrochim. Acta 213 (2016) 672–679.

[22] J. He, Y. Chen, P. Li, F. Fu, Z. Wang, W. Zhang, Self-assembled CoS_2 nanoparticles wrapped by CoS_2-quantum-dotsanchored graphene nanosheets as superior-capability anode for lithium-ion batteries, Electrochim. Acta 182 (2015) 424–429.

[23] P. Hasin, Electrochemical milling process to synthesize amorphous CoS as efficient electrocatalyst for the counter electrode of an efficient dye-sensitized solar cell, Sol. Energy 135 (2016) 398–407.

[24] L. Shao, X. Wang, B. Yang, Q. Wang, Q. Tian, Z. Ji, J. Zhang, A highly sensitive ascorbic acid sensor based on hierarchical polyaniline coated halloysit nanotube prepared by electrophoretic deposition, Electrochim. Acta 255 (2017) 286–297.

[25] L. Yang, L. Xie, X. Ren, Z. Wang, Z. Liu, G. Du, A.M. Asiri, Y. Yao, X. Sun, Hierarchical $CuCo_2S_4$ nanoarrays for high-efficient and durable water oxidation electrocatalysis, Chem. Commun. 54 (2018) 78–81.

[26] C. Su, J. Xiang, F. Wen, L. Song, C. Mu, D. Xu, C. Hao, Z. Liu, Microwave synthesized three-dimensional hierarchical nanostructure CoS_2/MoS_2 growth on carbon fiber cloth: a bifunctional electrode for hydrogen evolution reaction and supercapacitor, Electrochim. Acta 212 (2016) 941–949.

[27] H.S. Jadhav, A. Roy, G.M. Thorat, W.J. Chung, J.G. Seo, Hierarchical free-standing networks of $MnCo_2S_4$ as efficient Electrocatalyst for oxygen evolution reaction, J. Ind. Eng. Chem. 71 (2019) 452–459.

[28] X. Wang, L. Xu, K. Song, R. Yang, L. Jia, X. Guo, X. Jing, J. Wang, Synthesis of $MnCo_2O_4$@$MnCo_2S_4$ core/shell micro-nanostructures on Ni foam for high performance asymmetric supercapacitors, Colloid. Surface. 570 (2019) 73–80.

[29] H. Wang, K. Zhang, Y. Song, J. Qiu, J. Wu, L. Yan, $MnCo_2S_4$ nanoparticles anchored to N- and S-codoped 3D graphene as a prominent electrode for asymmetric supercapacitors, Carbon 146 (2019) 420–429.

[30] X. Li, J. Ouyang, Y. Zhou, H. Yang, Assembling strategy to synthesize palladium modified kaolin nanocomposites with different morphologies, Sci. Rep. 5 (2015) 13763–13774.

[31] X. Li, Q. Yang, J. Ouyang, H. Yang, S. Chang, Chitosan modified halloysite nanotubes as emerging porous microspheres for drug carrier, Appl. Clay Sci. 126 (2016) 306–312.

[32] H.-J. Kim, H.D. Lee, S.S. Rao, A.E. Reddy, S.K. Kim, C.V. Thulasi-Varma, Well-dispersed NiS nanoparticles grown on a functionalized CoS nanosphere surface as a high performance counter electrode for quantum dot sensitized solar cells, RSC Adv. 6 (2016) 29003–29019.

[33] Z. Wang, M. Jiang, J. Qin, H. Zhou, Z. Ding, Reinforced photocatalytic reduction of CO_2 to CO by a ternary metal oxide $NiCo_2O_4$, Phys. Chem. Chem. Phys. 17 (2015) 16040–16046.

[34] H. Kang, X. Liu, S. Zhang, J. Zhang, Functionalization of halloysite nanotubes (HNTs) via mussel-inspired surface modification and silane grafting for HNTs/soy protein isolate nano composite film preparation, RSC Adv. 7 (2017) 24140–24148.

[35] M. Zheng, H. Zhang, X. Gong, R. Xu, Y. Xiao, H. Dong, X. Liu, Y. Liu, A simple additive-free approach for the synthesis of uniform manganese monoxide nanorods with large specific surface area, Nanoscale Res. Lett. 8 (2013) 166–173.

[36] M. Zheng, Y. Liu, K. Jiang, Y. Xiao, D. Yuan, Alcohol-assisted hydrothermal carbonization to fabricate spheroidal carbons with a tunable shape and aspect ratio, Carbon 48 (2010) 1224–1233.

[37] H. Chen, J. He, Facile synthesis of monodisperse manganese oxide nanostructures and their application in water treatment, J. Phys. Chem. C 112 (2008) 17540–17545.

[38] E. Vijayakumar, A. Subramania, Z. Fei, P.J. Dyson, High-performance dye-sensitized solar cell based on an electrospun poly(vinylidene fluoride-cohexafluoropropylene)/cobalt sulfide nanocomposite membrane electrolyte, RSC Adv. 5 (2015) 52026–52032.

[39] M. Sevilla, A.B. Fuertes, Chemical and structural properties of carbonaceous products obtained by hydrothermal carbonization of saccharides, Chem. Eur J. 15 (2009) 4195–4203.

[40] Y. Zhang, X. He, J. Ouyang, H. Yang, Palladium nanoparticles deposited on silanized halloysite nanotubes: synthesis, characterization and enhanced catalytic property, Sci. Rep. 3 (2013) 2948–2954.

[41] E. Abdullayev, A. Joshi, W. Wei, Y. Zhao, Y. Lvov, Enlargement of halloysite clay nanotube lumen by selective etching of aluminum oxide, ACS Nano 6 (2012) 7216–7226.

[42] Z. Luo, A. Wang, C. Wang, W. Qin, N. Zhao, H. Song, J. Gao, Liquid crystalline phase behavior and fiber spinning of cellulose/ionic liquid/halloysite nanotubes dispersions, J. Mater. Chem. A 2 (2014) 7327–7336.

[43] Y.M. Lvov, D.G. Shchukin, H. Möhwald, R.R. Price, Halloysite clay nanotubes for controlled release of protective agents, ACS Nano 2 (2008) 814–820.

[44] S.K. Shinde, M.B. Jalak, G.S. Ghodake, N.C. Maile, V.S. Kumbhar, D.S. Lee, V.J. Fulari, D.-Y. Kim, Chemically synthesized nanoflakes-like $NiCo_2S_4$ electrodes for high-performance supercapacitor application, Appl. Surf. Sci. 466 (2019) 822–829.

[45] S.K. Shinde, D.P. Dubal, G.S. Ghodake, V.J. Fulari, Hierarchical 3D-flower-like CuO nanostructure on copper foil for supercapacitors, RSC Adv. 5 (2015) 4443–4447.

[46] S.K. Shinde, D.P. Dubal, G.S. Ghodake, D.Y. Kim, V.J. Fulari, Nanoflower-like $CuO/Cu(OH)_2$ hybrid thin films: synthesis and electrochemical supercapacitive properties, J. Electroanal. Chem. 732 (2014) 80–85.

[47] S. Shinde, H. Dhaygude, D.-Y. Kim, G. Ghodake, P. Bhagwat, P. Dandge, V. Fulari, Improved synthesis of copper oxide nanosheets and its application in development of supercapacitor and antimicrobial agents, J. Ind. Eng. Chem. 36 (2016) 116–120.

[48] S.K. Shinde, D.-Y. Kim, G.S. Ghodake, N.C. Maile, A.A. Kadam, D.S. Lee, M.C. Rath, V.J. Fulari, Morphological enhancement to CuO nanostructures by electron beam irradiation for biocompatibility and electrochemical performance, Ultrason. Sonochem. 40 (2018) 314–322.

[49] Z. Tang, C.-H. Tang, H. Gong, A High energy density asymmetric supercapacitor from nano-architectured $Ni(OH)_2$/Carbon nanotube electrodes, Adv. Funct. Mater. 22 (2012) 1272–1278.

[50] S. Liu, S.C. Jun, Hierarchical manganese cobalt sulfide core shell nanostructures for high-performance asymmetric supercapacitors, J. Power Sources 342 (2017) 629–637.

[51] Y. Li, L. Cao, L. Qiao, M. Zhou, Y. Yang, P. Xiao, Y. Zhang, Ni–Co sulfide nanowires on nickel foam with ultrahigh capacitance for asymmetric supercapacitors, J. Mater. Chem. A 2 (2014) 6540–6548.

[52] W. Chen, C. Xia, H.N. Alshareef, One step electrodeposited nickel cobalt sulfide nanosheet arrays for high-performance asymmetric supercapacitors, ACS Nano 8 (2014) 9531–9541.

[53] L. Shen, L. Yu, H.B. Wu, X.Y. Yu, X. Zhang, X.W. Lou, Formation of nickel cobalt sulfide ball-in-ball hollow spheres with enhanced electrochemical pseudocapacitive properties, Nat. Commun. 6 (2014) 6694–6702.

[54] X. Yang, L. Zhao, J. Lian, Arrays of hierarchical nickel sulfides/MoS_2 nanosheets supported on carbon nanotubes backbone as advanced anode materials for asymmetric supercapacitor, J. Power Sources 343 (2017) 373–382.

[55] B. Guan, Y. Li, B. Yin, K. Liu, D. Wang, H. Zhang, C. Cheng, Synthesis of hierarchical NiS microflowers for high performance asymmetric supercapacitor, Chem. Eng. J. 308 (2017) 1165–1173.

[56] T. He, S. Wang, F. Lu, M. Zhang, X. Zhang, L. Xu, Controllable synthesis of hierarchical $NiCo_2S_4$@Ni_3S_2 core–shell nanotube arrays with excellent electrochemical performance for aqueous asymmetric supercapacitors, RSC Adv. 6 (2016) 97352–97362.